Check for updates

Inverse 'intra-lattice' charge transfer in nickel–molybdenum dual electrocatalysts regulated by under-coordinating the molybdenum center†

Sahanaz Parvin,[a] Neha Bothra,[b] Supriti Dutta,[b] Mamoni Maji,[a] Maglu Mura,[a] Ashwani Kumar,[a] Dhirendra K. Chaudhary,[ac] Parasmani Rajput,[de] Manvendra Kumar,[f] Swapan K. Pati[b] and Sayan Bhattacharyya [*a]

The prevalence of intermetallic charge transfer is a marvel for fine-tuning the electronic structure of active centers in electrocatalysts. Although Pauling electronegativity is the primary deciding factor for the direction of charge transfer, we report an unorthodox intra-lattice 'inverse' charge transfer from Mo to Ni in two systems, $Ni_{73}Mo$ alloy electrodeposited on Cu nanowires and NiMo-hydroxide (Ni : Mo = 5 : 1) on Ni foam. The inverse charge transfer deciphered by X-ray absorption fine structure studies and X-ray photoelectron spectroscopy has been understood by the Bader charge and projected density of state analyses. The undercoordinated Mo-center pushes the Mo 4d-orbitals close to the Fermi energy in the valence band region while Ni 3d-orbitals lie in the conduction band. Since electrons are donated from the electron-rich Mo-center to the electron-poor Ni-center, the inverse charge transfer effect navigates the Mo-center to become positively charged and *vice versa*. The reverse charge distribution in $Ni_{73}Mo$ accelerates the electrochemical hydrogen evolution reaction in alkaline and acidic media with 0.35 and 0.07 s^{-1} turnover frequency at -33 ± 10 and -54 ± 8 mV *versus* the reversible hydrogen electrode, respectively. The corresponding mass activities are 10.5 ± 2 and 2.9 ± 0.3 A g^{-1} at 100, and 54 mV overpotential, respectively. Anodic potential oxidizes the Ni-center of NiMo-hydroxide for alkaline water oxidation with 0.43 O_2 s^{-1} turnover frequency at 290 mV overpotential. This extremely durable homologous couple achieves water and urea splitting with cell voltages of 1.48 ± 0.02 and 1.32 ± 0.02 V, respectively, at 10 mA cm^{-2}.

[a]*Department of Chemical Sciences and Centre for Advanced Functional Materials, Indian Institute of Science Education and Research (IISER) Kolkata, Mohanpur, 741246, India. E-mail: sayanb@iiserkol.ac.in*

[b]*Theoretical Sciences Unit, School of Advanced Materials, Jawaharlal Nehru Centre for Advanced Scientific Research, Bangalore 560064, India*

[c]*Centre for Renewable Energy, Prof. Rajendra Singh (Rajju Bhaiya) Institute of Physical Sciences for Study and Research, V. B. S. Purvanchal University, Jaunpur 222003, India*

[d]*Beamline Development and Application Section, Bhabha Atomic Research Center, Trombay, Mumbai 400085, India*

[e]*Homi Bhabha National Institute, Anushakti Nagar, Mumbai-400094, India*

[f]*Department of Physics, Institute of Science, Shri Vaishnav Vidyapeeth Viswavidyalaya, Indore, 453111, India*

† Electronic supplementary information (ESI) available: XRD patterns of control samples; Rietveld refinement data; W–H plot; strain calculation; elemental analyses by HAADF-STEM; FESEM images; CV plots; XPS spectra; LSV curves of control samples; ECSA determination; ECSA normalized plots; GC plot; mass activity plots; EIS parameters; TOF plots; Tafel, Nyquist and faradaic efficiency plots; reproducibility; post-stability characterization; computational model and tables of 2θ values; Bader charge density; Ni–Mo bond distances in Ni_4Mo, free energy diagram for the OER, electronic adsorption energy for the UOR; free energy calculations of Ni(111) and Pt(111); scatter plots of overpotentials. See DOI: https://doi.org/10.1039/d2sc04617b

Introduction

The success of implementing alternative energy resources on a global scale largely depends on the choice of material systems that catalyze the redox processes in electrochemical energy conversion and storage devices.[1] The activity modulation of these electrocatalysts is governed by the regulation of their electronic structure, in which intramolecular and intermolecular charge transfer plays a key role.[2] Charge transfer is commonly induced by heteroatom doping, defect density modifications, altering the single atom coordination or by changing the surface molecular functionalization. The most familiar occurrence is charge redistribution between the metal and non-metal,[3,4] due to their disparate electronegativity (EN), which is the power of an atom to attract electrons in a given orbital towards itself.[5,6] The rule of thumb is the acceptance of electrons by an atom with a vacant orbital from a neighboring atom with a filled orbital, to stabilize its eigen state.[7] Based on the Pauling EN scale, charge is transferred from a less EN to a more EN component, governed by its electrochemical potential.

Likewise, interfacial electronic distribution during metal-to-metal charge transfer in heterojunctions alters the electron density of metal centers.[8,9] In composites, this can initiate

electronic coupling between the components, modulating the metal valence states.[10] For instance, Co is more positive in Co-coordinated N-rich Mo_5N_6, since the EN of Co and Mo is 1.88 and 2.16, respectively.[8] Charge transfer occurs from NiCo-LDH to 1T-WS_2 in a 2D heterostructure, since the EN of Co (1.88) and Ni (1.91) is lower than W (2.36).[9] Intermetallic charge transfer often leads to an asymmetric electronic distribution at the catalytically active metal centers, impacting the adsorption and desorption of reaction intermediates.[11–13] In addition, the catalyst–support charge transfer interactions also influence the overall reactivity.[14,15]

Charge transfer follows this directive unless it is overpowered by an opposing voltage bias, for example, during reduction, electron transfer occurs from more EN substrates such as Ni foam and carbon to less EN metal components of the catalyst.[13,18] In the absence of an external driving force, reversing the path of charge transfer is apparently incongruous. Instances where the charge transfer is reversed because of the intrinsic electronic properties of the constituent atoms are in fact rare.[14,19,20] Some of the cases in point are the dependence of charge transfer on the size of the metal entity, where reverse charge transfer occurs from the S-doped carbon support to Pt only when the latter exists as single atoms.[14] A similar reversal of charge transfer has been observed from oxygen vacancy-rich TiO_2 to anchored Pt nanoclusters,[19] and from gold to annealed copper phthalocyanine films.[20] However, the available examples relate only to catalyst–support interactions.

Our study is based on the unusual observation of an intrinsic, intra-lattice, inverse charge transfer from Mo to Ni both in their metallic state as well as the higher oxidation states, and the implications of this inverse effect on their electrocatalytic performance. We have coined the term "intra-lattice" for the charge transfer occurring within the same lattice, in order to differentiate it from the "inter-lattice" charge transfer processes that occur between two phases across the heterogeneous interfaces, or from the substrate to the catalyst under the influence of applied potential. The electronic interaction through an "intra-lattice" charge transfer can occur either between two metal centers in an alloy or between the metal and ligand.[16,17] The Ni–Mo alloy is a celebrated hydrogen evolution reaction (HER) catalyst but with a stipulated Ni : Mo ratio of 4 : 1.[21] The conventional addition of 20% Mo offers a favorable hydrogen adsorption-free energy at the Ni-sites[22] and maneuvers the d-band electron density to regulate the rate of hydrogen adsorption and desorption.[23] While the Ni–Mo combination is not very common for the anodic oxygen evolution reaction (OER)[24–30] the choice of Ni is always propitious for both the half-reactions. Ni has a lower free energy of adsorption of OER intermediates,[31] as well as the nominal interaction between O 2p of ·OH radicals and Ni 3d orbitals facilitates the desorption of H_2 from the Ni center.[32] The electronegativity of Mo is higher with respect to Ni in spite of its larger atomic size and atomic number than Ni since with an electronic configuration of [Kr] $4d^5 5s^1$, Mo has a tendency to attract electrons due to its vacant s-orbital whereas Ni has a filled s orbital because of its electronic configuration of [Ar]$3d^8 4s^2$. We show that by lowering the

Mo-content in this bimetallic combination, the charge transfer direction contradicts the principle of Pauling electronegativity.

We deal with two systems, the $Ni_{73}Mo$ alloy electrodeposited on Cu nanowires (NW), and NiMo-hydroxide (Ni : Mo = 5 : 1) with Ni^{2+}, Ni^{3+}, Mo^{5+} and Mo^{6+} states, deposited on Ni foam. Because of the inverse charge transfer, the Mo-center attains a positive charge surrounded by the negatively charged Ni atoms. The adsorption of H_2O molecules on the Mo-center of $Ni_{73}Mo$ and the splitting of H_2O^* to $*OH$ and H^* on the neighboring Ni-centers accelerates the alkaline HER activity. In contrast, anodic potential increases the oxidation state of Ni in NiMo-hydroxide for water and urea oxidation reactions. The thermodynamic cell voltage for the urea oxidation reaction (UOR) is 0.37 V, which is 860 mV less than that of the OER (1.23 V). The UOR overpotential is regulated by the adsorption of urea on the catalyst surface, and the stabilization of CO^*, and NH^* intermediates.[33] However, challenges exist due to the complicated transfer of intermediates and multiple gas desorption steps for the $6e^-$ transfer that often limits its potential for H_2 production by urea splitting and for the treatment of urea-containing wastewater. The NiMo-hydroxide and $Ni_{73}Mo$ alloy stand out as OER and HER catalysts, respectively, delivering overall water splitting with a cell voltage of 1.48 V and urea splitting at 1.32 V to reach 10 mA cm^{-2} current density. Both these catalysts are extremely durable and the $Ni_{73}Mo$ alloy even shows a pH universal activity, thereby fulfilling nearly all the figures-of-merit of next-generation earth-abundant catalysts for the OER,[26,34–36] and HER,[13,15,21–23,37,38] and those having bifunctional activity.[21,27,39–41] The $Ni_{73}Mo$ (−) ‖ NMH-24 (+) couple also shows better or comparable activity than the known catalysts for the UOR and urea splitting.[42–51] We start the following section by introducing the systems, providing evidence for the intra-lattice inverse charge transfer and conclude by discussing the impact of this effect on the outstanding electrocatalytic ability of these two systems.

Results and discussion

Ni–Mo systems

The $Ni_{73}Mo$ alloy was prepared by electrodeposition from $Ni(SO_4)_2 \cdot 7H_2O$ and $(NH_4)_6Mo_7O_{24} \cdot 4H_2O$ salts at −100 mA cm^{-2} in chronopotentiometric mode over Cu NWs grown on Cu mesh (Fig. 1a).[15] Hereafter, the catalysts except $Ni_{73}Mo$ are abbreviated as M–J–t, where M is the metal, J is the electrodeposition current density and t is the electrodeposition time. The atomic radii of Ni and Mo are 125 and 140 pm, respectively, and the formation of an alloy with Mo expands the lattice volume of face-centered cubic (FCC) metallic Ni (JCPDS 04-0850) (Fig. 1b). Reciprocally, the (111) reflection is downshifted from $2\theta = 44.58°$ for Ni-100-60m, the Ni-only sample prepared without the Mo-salt, to 44.43° for $Ni_{73}Mo$ (Fig. 1c and Table S1†). Rietveld refinement of the X-ray diffraction (XRD) pattern suggests an increase in lattice volume by 2.3 ± 0.02% (Fig. S1 and Table S2†). Characteristic Mo reflections are indiscernible in Fig. 1c because of its 1/74th fraction in the alloy. The Rietveld refined data showing a smaller fraction of Mo are substantiated by inductively coupled plasma optical emission spectroscopy (ICP-
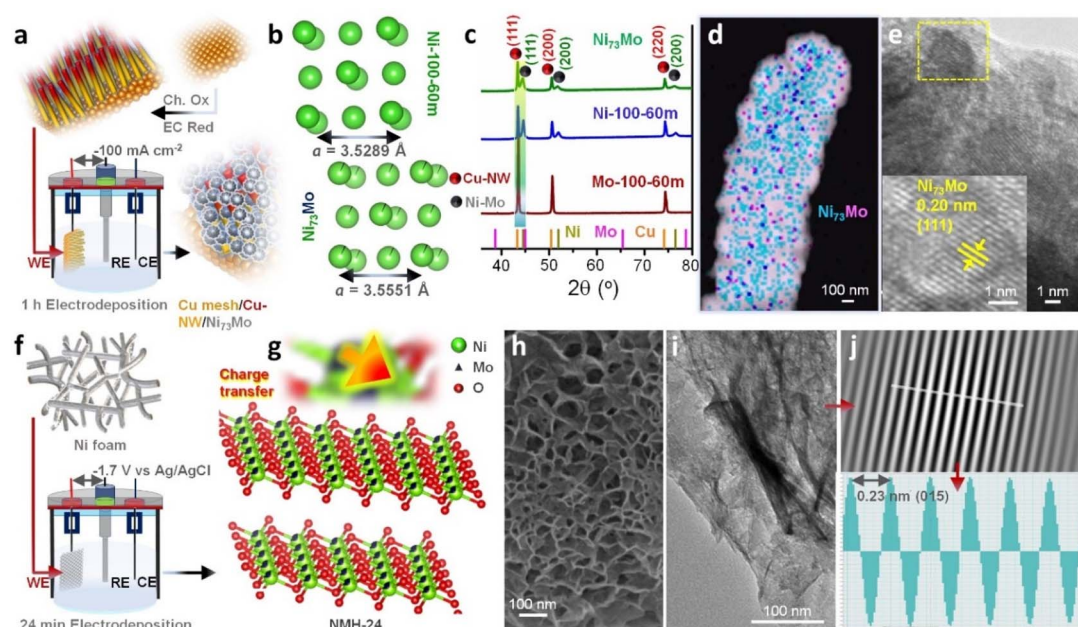
Fig. 1 Fabrication and characterization of $Ni_{73}Mo$ and NMH-24. (a) Schematic illustration of the fabrication of the $Ni_{73}Mo$ alloy at -100 mA cm^{-2} in chronopotentiometric mode on Cu-NW grown on Cu mesh. Ch. Ox is chemical oxidation and EC Red is electrochemical reduction. WE, RE and CE are the working, reference and counter electrodes, respectively. The electrolyte consists of an aqueous solution of 0.017 M $Ni(SO_4)_2\cdot7H_2O$, 0.016 M $Na_3C_6H_5O_7$, 0.36 mM $(NH_4)_6Mo_7O_{24}\cdot4H_2O$, 0.28 M NaCl and 27 wt% aqueous NH_3 solution (pH = 9.5). (b) Crystal structure representations of Ni-100-60m and $Ni_{73}Mo$, showing the increase in bond length due to Mo incorporation in the Ni lattice. (c) XRD patterns of $Ni_{73}Mo$, Ni-100-60m and Mo-100-60m, along with the standard patterns of individual metals. (d) Merged elemental map on the HAADF-STEM image of Cu-NW/$Ni_{73}Mo$, without Cu. (e) TEM image of $Ni_{73}Mo$ showing the 5.4 ± 1 nm quasi-spherical particles and the inset shows the (111) reflection in a single particle, magnified from the marked region. (f) Schematic illustration of the fabrication of the NMH-t on Ni foam at -1.7 V versus Ag/AgCl in chronoamperometric mode. The electrolyte consists of an aqueous solution of 0.04 M $NiCl_2\cdot6H_2O$, 0.0008 M $(NH_4)_6Mo_7O_{24}\cdot4H_2O$ and 0.04 M NH_4Cl. (g) Crystal structure representation of NMH-24, showing the charge transfer direction. The green and deep blue spheres represent Ni and Mo atoms, respectively. (h) Field-emission scanning electron microscope (FESEM) and (i) TEM images of NMH-24. (j) Mask filtered TEM of the (015) plane of NMH-24 and lattice fringe distribution plot showing $d_{015} = 0.23$ nm.

OES) and survey scan of X-ray photoelectron spectroscopy (XPS). ICP-OES and XPS analyses depict the Ni : Mo to be 73 : 1 (98.6% Ni, 1.4% Mo) and 80 : 1 (98.7% Ni, 1.3% Mo), respectively. Williamson–Hall (W–H) analysis shows the increase in lattice strain from 1.9×10^{-3} in Ni-100-60m to 4×10^{-3} after the incorporation of Mo in $Ni_{73}Mo$ (Fig. S2†).[52] With the help of transmission electron microscopy (TEM), the geometric-phase analysis (GPA) could map the spatial distribution of the lattice strain components. The E_{yy} component along the (111) plane shows the expansive lattice strain induced by Mo while the E_{xx} component, perpendicular to the (111) plane, corresponds to the shear strain (Fig. S2c and d†).[33] From the morphological perspective, the 140 ± 20 nm thick Cu NWs widen to 620 ± 70 nm after electrodeposition of $Ni_{73}Mo$ particles (Fig. S3†). Elemental mapping by high-angle annular dark-field scanning TEM (HAADF-STEM) shows a dense and uniform coverage of the alloy particles around the NWs (Fig. 1d and S4†). The TEM image in Fig. 1e discerns the average diameter of these quasi-spherical particles to be 5.4 ± 1 nm, whose lattice fringes correspond to the most intense (111) reflection having 0.2 nm interplanar spacing (Fig. S5†).

Our second system i.e. NiMo-hydroxide (Ni : Mo = 5 : 1) was electrodeposited in chronoamperometric mode on Ni foam at -1.7 V versus Ag/AgCl for different time periods (NMH-t, where t

is growth time in minutes), from $NiCl_2\cdot6H_2O$ and $(NH_4)_6Mo_7O_{24}\cdot4H_2O$ (Fig. 1f). In the representative NMH-24 sample, the (012) and (015) XRD reflections at $2\theta = 34.33°$ and $38.25°$, respectively, are in accordance with the hexagonal hydrotalcite type layered double hydroxide (LDH) (Fig. S6a and b†), the crystal structure of which is shown in Fig. 1g. This is distinctly different from the (100) and (101) reflections of the β-nickel hydroxide structure of NH-24, the sample prepared with Ni-only precursor. NMH-24 nanosheets have an intricate network (Fig. 1h) with extended lateral dimensions (Fig. 1i), which increase gradually as a function of the electrodeposition time (Fig. S6c–f†). Individually, Mo-hydroxide (MH-24, the sample prepared with the Mo-only precursor) has a 150 nm wide flowery morphology and NH-24 has nanosheets of 522 nm spread (Fig. S6g and h†). The fast Fourier transform (FFT) mask filter analysis from a selected region in Fig. 1i reveals the d-spacing of 0.23 nm corresponding to the (015) LDH reflection (Fig. 1j).

Inverse charge transfer

The first evidence of intrinsic inverse charge transfer from Mo to Ni in $Ni_{73}Mo$ and NMH-24 stems from our analysis of X-ray absorption fine structure (XAFS), shown in Fig. 2 and S7.† The first derivative plots in X-ray absorption near edge structure (XANES) of $Ni_{73}Mo$ and Ni-100-60m show two major peaks,
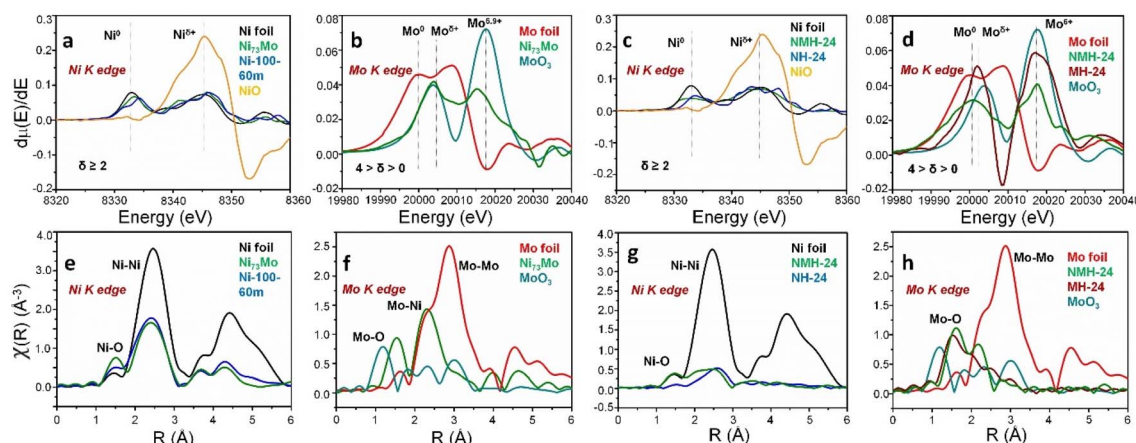
Fig. 2 XAFS analyses of the inverse charge transfer in $Ni_{73}Mo$ and NMH-24. The first derivative of XANES spectra at (a) Ni K edge for $Ni_{73}Mo$, Ni foil, NiO, and Ni-100-60m, (b) Mo K edge for $Ni_{73}Mo$, Mo foil, and MoO_3, (c) Ni K edge for NH-24, NMH-24, Ni foil, and NiO, and (d) Mo K edge for NMH-24, MH-24, MoO_3, and Mo foil. The Fourier Transform of k^2-weighted $\chi(R)$ spectra (phase corrected) at (e) Ni K edge for $Ni_{73}Mo$, Ni foil, and Ni-100-60m, (f) Mo K edge for $Ni_{73}Mo$, Mo foil, and Mo-100-60m, (g) Ni K edge for NMH-24, NH-24, and Ni foil, and (h) Mo K edge for NMH-24, MH-24, Mo foil, and MoO_3.

where the energy at 8333 eV corresponds to Ni^0 and the 8345 eV peak is for $Ni^{\delta+}$ ($\delta \geq 2$).[53] The 8333 eV peak is closer to the binding energy of Ni foil reference, where the Ni^0 binding energy decreases from Ni-100-60m to $Ni_{73}Mo$, suggesting a more electron-dense Ni-center in the alloy (Fig. 2a) The XAFS analysis for Ni K edge shows a radial distance of 2.4 Å due to the Ni–Ni/Ni–Mo bond present in Ni-100-60m and $Ni_{73}Mo$, very close to the 2.5 Å Ni–Ni bond distance of Ni foil (Fig. 2e). Due to a paltry Mo content of $\sim$1.5% in the Ni lattice, the radial distance does not change noticeably between Ni-100-60m and $Ni_{73}Mo$. The electron-dense Ni-center is further corroborated by the Mo K edge spectrum of $Ni_{73}Mo$ which shows a positive shift of binding energy relative to the 19 999.8 eV Mo^0 peak of Mo foil reference (Fig. 2b). The Mo–Mo bond in Mo foil has a radial distance of 2.9 Å which decreases to 2.3 Å in the $Ni_{73}Mo$ alloy due to the presence of 98.5% Ni with a lower atomic radius than Mo (Fig. 2f). The $Ni^{\delta+}$ peak of NMH-24 shows a similar negative energy shift to that in NH-24, whereas the binding energy of $Mo^{5.9+}$ state increases from MH-24 to NMH-24, demonstrating the Mo $\rightarrow$ Ni charge transfer (Fig. 2c and d). For the Ni K edge XAFS spectra of NMH-24 and NH-24, the Ni–O and Ni–Ni bonds appear from the catalyst and Ni foam substrate, respectively (Fig. 2g). The Mo–O radial bond distance of NMH-24 and MH-24 is higher than that of the MoO_3 reference due to their different coordination environments (Fig. 2h).[54]

The XPS data in Fig. 3a–d provide the second evidence of this unconventional charge distribution. Each element in the survey spectra (Fig. S8†) was calibrated by the C 1s level (Fig. S9†). The Ni^0 binding energy of Ni $2p_{3/2}$ level shifts from 852.7 eV for Ni-100-60m to 852.4 eV for 20 nm Ar^+ sputtered $Ni_{73}Mo$, thereby discerning more electron density on Ni-sites in the alloy (Fig. 3a). The Mo^0 state of Mo $3d_{5/2}$ level conversely shifts in binding energy from 227.2 eV for Mo-100-60m (Mo-only sample) to 228.1 eV for $Ni_{73}Mo$ (Fig. 3b). The downshift of Ni^0 and upshift of Mo^0 binding energies from Ni-100-60m and Mo-100-60m to $Ni_{73}Mo$ clearly manifests the charge transfer from more

EN Mo to Ni. The higher valence Ni^{2+}, Ni^{3+}, Mo^{5+} and Mo^{6+} states appear due to surface oxidation of the alloy which is more prominent in the non-sputtered sample (Fig. S10a and b†). Since Cu has a high standard reduction potential of +0.34 V, the metallic state of Cu NWs is only marginally compromised by surface oxidation (Fig. S10c and d†). The higher valence states in NMH-24 also behave synchronously in accordance with the inverse charge transfer effect. The binding energy of the Ni^{2+} state is lowered from 855.0 eV for NH-24 to 854.2 eV for NMH-24 (Fig. 3c). The binding energy of the Ni^{3+} state is also shifted from 856.7 eV for NH-24 to 855.9 eV for NMH-24. When compared to MH-24 (Mo-hydroxide), the Mo^{5+} state is elevated from 230.8 eV to 231.0 eV for NMH-24 (Fig. 3d). The O 1s spectrum of NMH-24 consists of lattice oxygen from the LDH, defect oxygen, adsorbed OH^- and water (Fig. S10e†).

Cyclic voltammetry (CV) studies show that the electron-dense Ni centers stabilize the Ni^{2+} valence state more than Ni^{3+} (Fig. S11†). Under oxidative bias in 1 M KOH, firstly the Ni^{2+}/Ni^{3+} oxidation peak of NH-24 is shifted to higher potential in NMH-24, signifying the requirement of additional voltage for oxidation of the electron-dense Ni center. Secondly, the current density of this oxidation peak is more in the case of NMH-24 since a greater number of Ni^{2+} species had to be oxidized by the applied potential, rather than NH-24, where Ni^{3+} is more in abundance (NH-24: Ni^{2+}/Ni^{3+} = 1.4, NMH-24: Ni^{2+}/Ni^{3+} = 1.8, Fig. 3c). Mott–Schottky analysis in the potential range −0.93 to 3.2 V shows a shift in the flat-band potential (E_{fb}) from 2.1 V in NH-24 to 1.6 V in NMH-24, both with a p-type character (Fig. S12†). The negative shift of E_{fb} is also reflected in the slightly higher dopant density of 4.3×10^{11} in NMH-24 than 1.2×10^{11} in NH-24, under the oxidative bias.[55,56] The E_{fb} of NMH-24 is closer to 1.53 V versus the reversible hydrogen electrode (RHE), which is suitable for creating a hole accumulation layer at the anode–electrolyte interface for triggering the water oxidation process.[57]
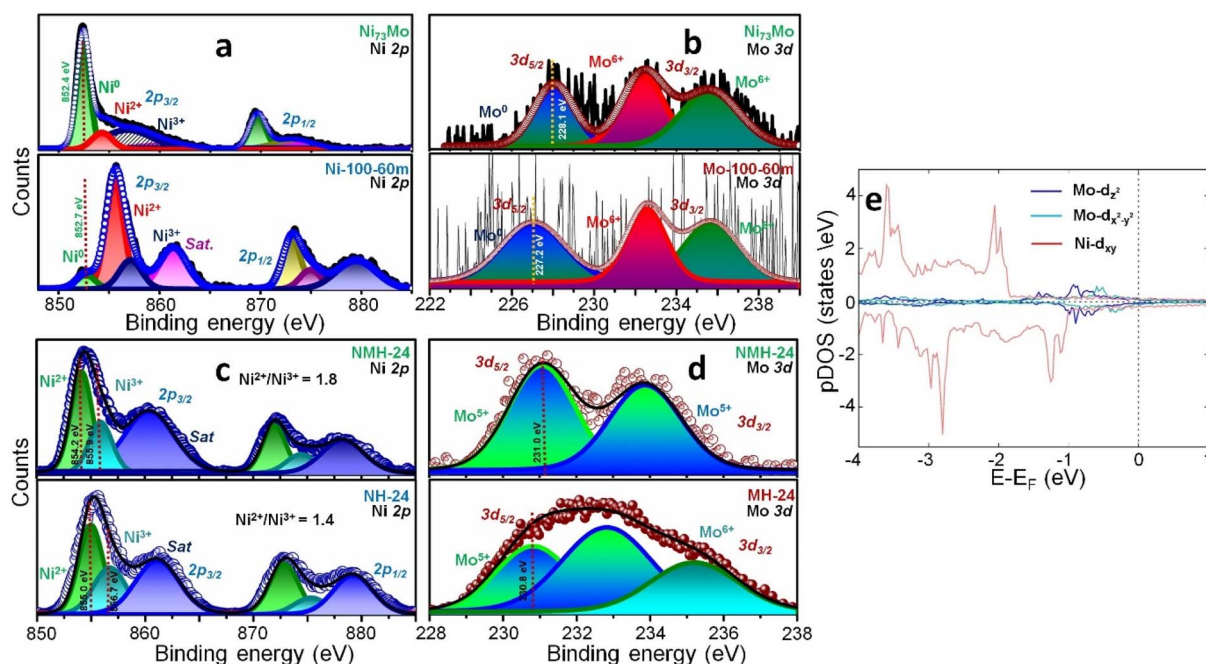
Fig. 3 XPS and computational analyses of the inverse charge transfer in $Ni_{73}Mo$ and NMH-24. Deconvoluted XPS of (a) Ni 2p level for 20 nm Ar^+ sputtered $Ni_{73}Mo$ and Ni-100-60m, (b) Mo 3d level for 20 nm Ar^+ sputtered $Ni_{73}Mo$ and Mo-100-60m, (c) Ni 2p level for NMH-24 and NH-24, and (d) Mo 3d level for NMH-24 and MH-24. (e) pDOS analyses of the Mo-center and neighboring six Ni-centers of Mo-doped Ni (111) in the modelled $Ni_{79}Mo$ system.

Computational studies by Bader charge analysis,[58–62] give us the reasoning of the experimentally observed inverse charge transfer in the $Ni_{73}Mo$ alloy.[63] A 4×4 Ni (111) surface was constructed with 6 layers consisting of 80 atoms. To replicate the stoichiometry, only a single Ni atom was substituted by Mo. Each surface metal of this $Ni_{79}Mo$ system including the Mo-center is 9 coordinated, although according to an earlier study, the Mo-center consists of an icosahedron structure with 12 coordination.[64] This suggests the fact that the Mo-center is capable of further bonding. Also, d-orbital analyses *via* projected density of states (pDOS) show that the doublet ($d_{x^2-y^2}$ and d_{z^2}) of the Mo-center is close to the Fermi energy (E_f) in the valence band region (Fig. 3e). There is a small contribution of d_{xy} (from six nearest Ni centers) and d_{z^2} (from three Ni centers in the second layer) which appear close to the Fermi energy in the conduction band region. The undercoordination of the Mo-center aligns its symmetry-adapted filled d-orbitals to remain in the valence band region close to the Fermi energy, while the local coordination of the Ni-centers aligns its frontier orbitals in the conduction band close to the Fermi energy. Such an alignment of the Mo and Ni orbitals in the low energy region results in the inverse charge transfer from the Mo-center to the Ni-centers. As a consequence, the Mo-center holds a positive charge while the surrounding six Ni-centers on the surface and three Ni-centers in the second layer are negatively charged. The calculated average charge density on nearby Ni atoms at the surface varies from $-0.12e$ to $-0.13e$, that on the Ni atoms in the second layer from $-0.08e$ to $-0.096e$, whereas Mo has a charge density of $1.10e$ (Table S3†). Each neighboring Ni-

center accepts only a very small amount of charge density from the Mo-center, which localizes the positive charge on the latter. Our analyses lead to the fact that although Mo has $4d^5 5s^1$ and Ni has $3d^8 4s^2$ electronic configurations, purely due to the local geometry in the Mo-doped Ni-rich clusters, the Mo-site is electron rich and donates it to Ni centers which act as electron-poor centers. In order to check the role of the Cu substrate on the charge transfer process, we have optimized the hetero-system with 3 layers of Cu below the $Ni_{79}Mo$ alloy. The reverse charge transfer effect with a positively charged Mo center remains unaltered even in the presence of an underlying Cu substrate. The charge transfer persists only at the interface between the alloy and the Cu substrate (Fig. S13†). With an underlying Cu, the atoms at the top layers in the $Ni_{79}Mo$ alloy do not participate in the charge transfer while the Mo atom at the top layer remains the active center. The reaction occurs at the top surface of the $Ni_{79}Mo$ system and the electronic nature of Mo remains the same.

To understand the dependence of the nature of charge transfer on the intermetallic ratio, computational calculations were performed with Ni : Mo ratios of 1 : 4 and 4 : 1 by optimizing the geometries (Fig. S14†). The former 1 : 4 configuration is unstable with multiple vibrational modes that become negative with imaginary wavevectors, because of which the structural parameters vary during geometric optimization and hence are not considered further. The $Ni_{64}Mo_{16}$ system with the Ni : Mo ratio of 4 : 1 consists of 5 layers with four Mo substituted at each of the first four layers, without any Mo in the fifth layer. While the $Ni_{79}Mo$ modelled system contains six equidistant Ni–

Mo (2.51 Å) bonds in the same layer and three equidistant Ni–Mo bonds (2.46 Å) from the next layer, $Ni_{64}Mo_{16}$ contains unequal bond lengths of 2.50–2.64 Å for the intralayer Mo center and 2.64–2.86 Å across the interlayer (Table S4†). These inequalities in bond length are consistent for the Mo-center from the second layer as well. Thus, on increasing the Mo content from Ni : Mo 79 : 1 to 4 : 1, Mo always remains undercoordinated in the absence of an effective local icosahedron geometry,[64] albeit with more variations in the bond strength. Bader charge analyses of $Ni_{64}Mo_{16}$ also show that the undercoordinated Mo-centers are positively charged, due to Mo → Ni charge transfer (Table S5†). The computational results were experimentally verified by reproducing a well-known HER catalyst, Ni_4Mo/MoO_2 (Fig. S15 and S16†).[22] The reproduced Ni_4Mo/MoO_2 microrods contain zerovalent metals along with the oxidized states of Ni^{2+}, Ni^{3+}, Mo^{4+} and Mo^{6+}. Although the Ni^0 binding energy of Ni_4Mo/MoO_2 in the XANES analysis is lower than that of Ni-100-60m, the Mo^0 binding energy also shows a negative energy shift than the Mo foil reference. In Ni_4Mo/MoO_2, charge transfer is experimentally indiscernible due to the presence of a surface oxide coverage over Ni_4Mo.

Electrochemical HER activity of the Cu mesh/Cu-NW/Ni_{73}Mo electrode

The electrocatalytic HER activity of the Cu mesh/Cu-NW/Ni_{73}Mo self-supported electrode was evaluated both in 1 M KOH and 0.5 M H_2SO_4 electrolytes at 1 mV s^{-1} scan rate, with a catalyst mass loading of 4 mg cm^{-2}. In an alkaline medium, we have used a three-electrode setup consisting of a self-supported

working electrode, Hg/HgO reference electrode and graphite rod counter electrode. The electrodes were stabilized and saturated by several CV cycles, before recording the LSV polarization curves (Fig. S17†). In 1 M KOH, Ni_{73}Mo exhibits an outstanding HER activity with a turnover frequency (TOF) of 0.35, 3.9 and 12.4 H_2 s^{-1} at 33, 150 and 250 mV, respectively (Fig. S18a†), and mass activity of 10.5 ± 2 A g^{-1} at −100 mV versus RHE (Fig. S19a†). 9 mL h^{-1} H_2 could be produced at −138 mV versus RHE with a 0.25 cm^2 electrode (Fig. S19b†). The faradaic efficiency is near 100%, attesting to a near-complete electrical to chemical energy conversion (Fig. S18b†).

A comparative analysis can be made in terms of overpotential as an acceptable extrinsic parameter.[65] The HER overpotentials of Ni_{73}Mo in 1 M KOH are 33 ± 10 mV at −10 mA cm^{-2} and 142 ± 15 mV at −100 mA cm^{-2} (Fig. 4a and b). To ensure the reliability of the data and avoid any reduction peak from the metals, the HER overpotential of Ni_{73}Mo in 1 M KOH was also verified by the LSV polarization in backward scan mode at 1 mV s^{-1} scan rate, which shows an overpotential of 25, and 117 mV to reach −10, and −100 mA cm^{-2}, respectively (Fig. S17c†). Moreover, the HER overpotential of Ni_{73}Mo in 1 M KOH was further checked by chronopotentiometry at −10 mA cm^{-2} for 1 h (Fig. S17e†). This extrinsic activity is better than the benchmark 20% Pt/C with the same catalyst loading at high current density but comparable at lower current density. Cu mesh/Cu-NW/Ni_{73}Mo being a self-supported current collector retains an uninterrupted mass diffusion even at larger applied potential, whereas the binder-assisted drop-casting of commercial Pt/C on Cu mesh hinders the mass diffusion by accumulation of bubbles under increased potential bias. Ni-
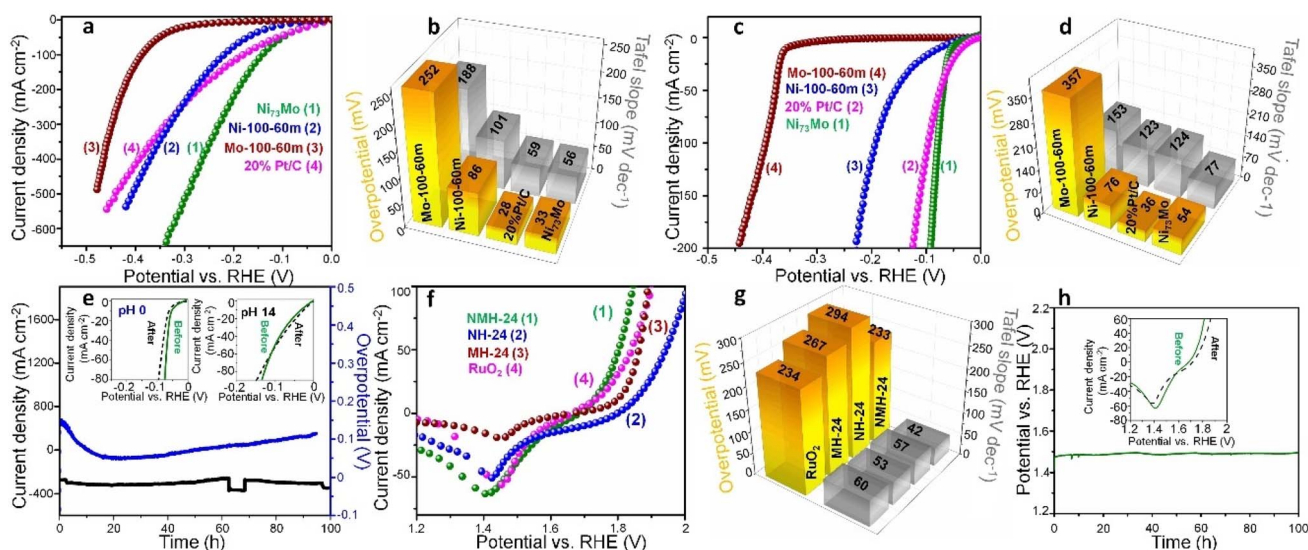

Fig. 4 Ni_{73}Mo and NMH-24 catalyzed redox half-reactions. (a) HER polarization curves (iR-corrected) in 1 M KOH for Ni_{73}Mo, Ni-100-60m, Mo-100-60m and 20% Pt/C. (b) Bar plots for overpotentials at −10 mA cm^{-2} and Tafel slopes in 1 M KOH. (c) HER polarization curves (iR-corrected) in 0.5 M H_2SO_4 for Ni_{73}Mo, Ni-100-60m, Mo-100-60m and 20% Pt/C. (d) Bar plots for overpotentials at −10 mA cm^{-2} and Tafel slopes in 0.5 M H_2SO_4. (e) Chronoamperometry and chronopotentiometry tests of Ni_{73}Mo for 100 h and 95 h at −0.534 V versus RHE and −100 mA cm^{-2} in 1 M KOH and 0.5 M H_2SO_4, respectively. The insets show steady-state LSV plots before and after the stability tests. (f) OER polarization curves (iR-corrected) in 1 M KOH for NMH-24, NH-24, MH-24 and RuO_2. (g) Bar plots for overpotentials at 10 mA cm^{-2} and Tafel slopes in 1 M KOH. (h) Chronopotentiometric stability test of NMH-24 for 100 h at 20 mA cm^{-2} in 1 M KOH. The insets show steady-state LSV plots before and after the stability test.

100-60m and Mo-100-60m require higher overpotentials of 86 and 252 mV at -10 mA cm^{-2}. The control samples based on variations of the current density and time of electrodeposition further attest to the superiority of the Ni$_{73}$Mo electrocatalyst (Fig. S18c and d†). Ni$_{73}$Mo has the lowest Tafel slope of 56 ± 13 mV dec^{-1} in alkaline HER (Fig. 4b and S18e†) indicating better intrinsic reaction kinetics.[21] The Tafel slope value of Ni$_{73}$Mo obtained from the LSV polarization in backward scan mode exhibits an unaltered HER mechanism (Fig. S17d†). While the electron-dense Ni active sites aid the Volmer step,[15] the minimal presence of Mo increases the strain in the FCC Ni lattice, which has positively influenced the electrocatalytic activity.[66] When the LSV polarization curves are normalized by electrochemically active surface area (ECSA), Ni$_{73}$Mo shows better intrinsic activity than Ni-100-60m (Fig. S20†). Electrochemical impedance spectral (EIS) analysis shows the fastest charge transfer for Ni$_{73}$Mo (Fig. S18f and Table S6†). The HER activity of Ni$_{73}$Mo in 1 M KOH is better or comparable with that of previously reported Ni–Mo catalysts with a lower Ni : Mo ratio (Fig. S21a†),[21–25,37,67–72] Ni–Mo-based trimetallic catalyst,[73] or with reported non-Ni-Mo systems (Fig. S21b†).[13,33] Also, since Mo is less abundant in the Earth's crust (28%) than with respect to Ni (68%), the incorporation of nominal Mo in our case is commercially lucrative.

The acidic HER activity was evaluated with a Pt wire and calomel electrode as counter and reference electrodes, respectively. Ni$_{73}$Mo performs equally well in 0.5 M H$_2$SO$_4$, requiring only 54 ± 8 mV to reach -10 mA cm^{-2} which is comparable with 20 wt% Pt/C (Fig. 4c and d). Here, the TOF is 0.07 and 1.7 H$_2$ s^{-1} at 54 and 100 mV, respectively (Fig. S22†), and the mass activity is 2.9 ± 0.3 A g^{-1} -54 mV *versus* RHE, with a Tafel slope of 77 ± 13 mV dec^{-1} (Fig. 4d and S18g†). Although reports on the acidic HER activity of Ni–Mo catalysts are scarce, this activity is found comparable with the available literature on Ni–Mo-based systems (Fig. S21c†),[74–78] and non-Ni-Mo catalysts (Fig. S21d†). Fig. 4e demonstrates the excellent durability of Ni$_{73}$Mo in both alkaline and acidic media. In 1 M KOH, the catalyst is stable for at least 100 h at a constant voltage of -0.534 V *versus* RHE (*iR*-uncorrected) with slight activity decay at high current densities. Inductively coupled plasma-mass spectrometry (ICP-MS) data shows the change in Ni : Mo atomic ratio as 32 : 1 after 100 h. In 0.5 M H$_2$SO$_4$, it is stable for at least 95 h at -100 mA cm^{-2} without any decay. The LSV polarization curves overlap before and after the stability tests. Different batches of Cu mesh/Cu-NW/Ni$_{73}$Mo self-supported electrodes demonstrate a reproducible HER activity in both alkaline and acidic electrolytes (Fig. S18h†). The characterization data of Ni$_{73}$Mo were reproduced with the samples synthesized in multiple batches, and the catalyst durability in alkaline medium was verified with each batch, separately with Pt wire and graphite rod counter electrodes (Fig. S23†).

The active sites of Ni$_{73}$Mo were elucidated from the free energy calculations using density functional theory (DFT). The free energy of adsorption of the proton, ΔG_{H*} has been the key descriptor for the HER in an acidic medium. However, the HER in an alkaline medium requires consideration of additional Volmer steps *i.e.* adsorption and splitting of the H$_2$O molecule, the pathways of which are shown in Fig. 5a. We have carried out the

thermodynamic analysis of each possible step of HER in an alkaline medium starting from adsorption of H$_2$O (H$_2$O*), followed by adsorption of split H$_2$O (H* + OH$^-$) and each individual intermediate (H* and OH*). Here, * represents the adsorbed species on the catalyst surface. Furthermore, the Evans–Polanyi principle (or Bell–Evans–Polanyi principle) has shown a linear relationship between the activation energy (ΔE_A) and enthalpy of the reaction (ΔH). After considering all the possible sites, *i.e.* Mo-top, nearest Ni- and next nearest Ni-top (Fig. 5b), it is found that the adsorption of the H$_2$O molecule occurs on each site but the Mo-center has shown the most exothermic adsorption. Interestingly, we found that the next step *i.e.* adsorption of split H$_2$O (H* + OH*) is preferably adsorbed on the Mo-center ($\Delta G = -0.12$ eV) followed by the next nearest Ni-center (-0.04 eV). It has been also observed that the OH* intermediate will preferably get adsorbed only on the Mo-center, which is due to its positive charge. In the case of proton adsorption, there is a presence of multiple active sites including the nearest and next-nearest Ni-centers. With this, the DFT analysis explains the experimental findings, with the inference that the H$_2$O* dissociation step is facilitated on both the Mo-center and the next nearest Ni-center at the Ni$_{79}$Mo catalyst surface.

In order to compare our results with other catalysts, we have additionally carried out thermodynamic calculations for Ni(111) and Pt(111) surfaces (Fig. S24 and Table S7†). The free energy of H$_2$O* adsorption on Ni(111) and Pt(111) surfaces is exothermic while the adsorption of OH* is mildly and strongly endothermic in nature (ΔG_{OH*} of 0.17 and 1.39 eV), respectively. However, since OH* is one of the intermediates after H$_2$O splitting, it should also be a favored adsorbed species. In contrast, in the Ni$_{79}$Mo system, the positively charged Mo-center and the nearest Ni-center are both advantageous for the adsorption of H* intermediate (ΔG_{H*} of -0.55 and -0.52 eV), respectively, whereas OH* adsorption is more preferable on Mo-center because of an exothermic binding ($\Delta G_{OH*} = -0.45$ eV). The OH* adsorption on the nearest Ni center is also exothermic ($\Delta G_{OH*} = -0.41$ eV) but on the next nearest Ni center, the adsorption of OH* is endothermic in nature ($\Delta G_{OH*} = 0.3$ eV). Hence, there is more than one active site present in Ni$_{79}$Mo. Although ΔG_{H2O*} (-0.23 eV) is most favorable on Pt(111) surface, the exothermic binding of OH* on the Mo-top and nearest Ni-center makes Ni$_{79}$Mo a better HER catalyst in an alkaline medium. The exothermic binding of OH* on Mo-top and its immediate vicinity has been made possible by the inverse charge transfer, which makes the Mo-center positively charged with a charge density of 1.10e. While in the case of acidic HER, H* is usually predominant, for alkaline HER, OH$^-$ is also the main species, and hence in our calculations, we have considered only the adsorption and splitting of the H$_2$O molecule according to the potential-determining Volmer step, along with the H* adsorption.

The free energy diagrams for alkaline HER for the computationally modelled Ni$_{79}$Mo alloy, Ni-100-60m and Mo-100-60m are compared in Fig. 5c. The initial H$_2$O adsorption is most exothermic in Ni$_{79}$Mo followed by Mo-100-60m and Ni-100-60m. For alkaline HER, the most crucial step is water dissociation which is more preferred on Ni$_{79}$Mo. Also, since OH* is one of
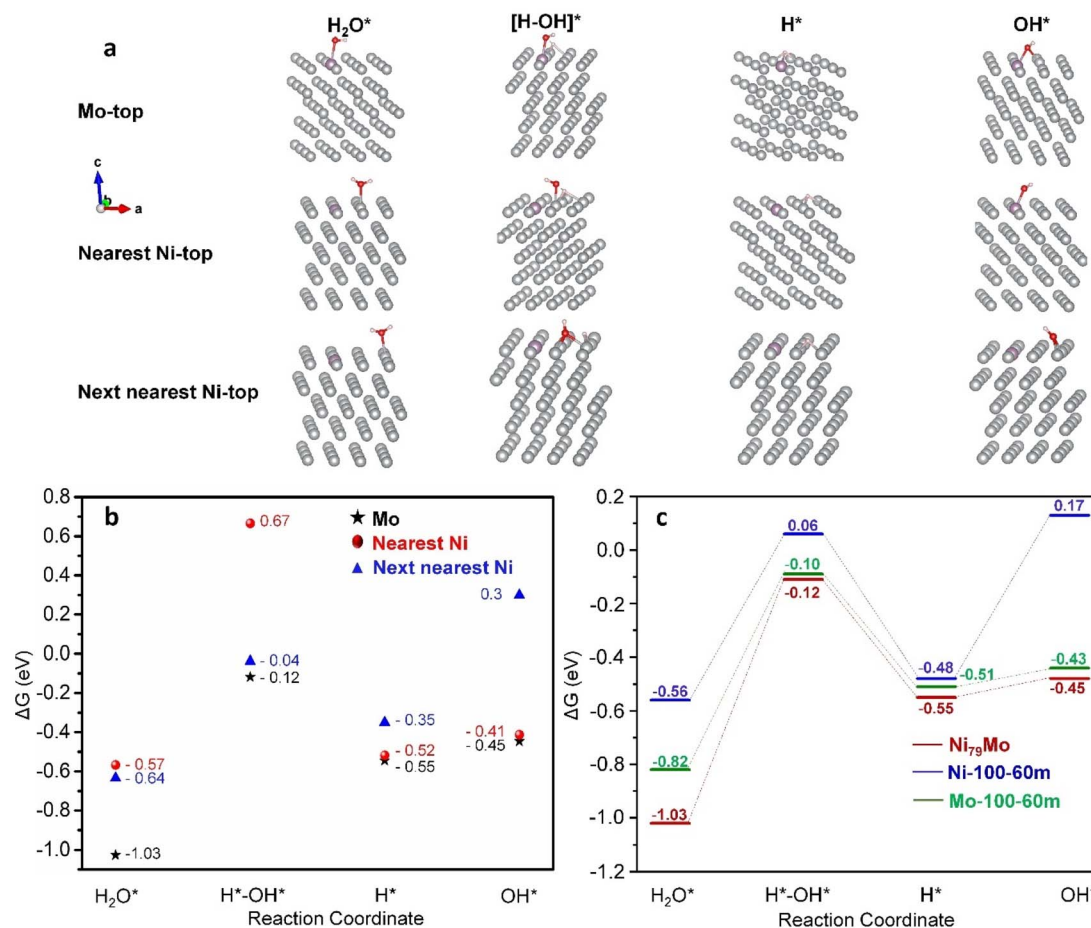
Fig. 5 Computational analyses for alkaline HER with the constructed $Ni_{79}Mo$, Ni-100-60m and Mo-100-60m. (a) Computational model showing the adsorption of different intermediates at Mo top (light pink spheres), nearest Ni top and next nearest Ni top (grey spheres). (b) Free energy diagram showing adsorption of different intermediates on different atoms (c) Free energy diagram for alkaline HER on $Ni_{79}Mo$, Ni-100-60m and Mo-100-60m.

the major intermediates in an alkaline medium, it should also be a favoured adsorbed species. The OH* adsorption is more exothermic in $Ni_{79}Mo$ as compared to Mo-100-60m, while it is endothermic for Ni-100-60m. A combination of all the steps shows that $Ni_{79}Mo$ has the most appropriate configuration for catalyzing the cathodic half-reaction.

Electrochemical OER activity of the Ni foam/NMH-24 electrode

The electrocatalytic OER activity of the Ni foam/NMH-24 self-supported electrode with a catalyst mass loading of 4.5 mg cm^{-2} was evaluated in 1 M KOH at 1 mV s^{-1} scan rate with a three-electrode setup consisting of a graphite rod counter electrode and Hg/HgO reference electrode. This catalyst has a TOF of 0.048, 0.43 and 2.32 O_2 s^{-1} at overpotentials of 234, 290 and 370 mV, respectively, along with 100% faradaic efficiency at 1.766 V (Fig. S25a and b†). The mass activity is 19 ± 8 A g^{-1} at 300 mV overpotential. Since the oxidative bias transforms the Ni^{2+} to Ni^{3+} states (Fig. S11†), NMH-24 has the highest ECSA, better than that of NH-24 and MH-24 (Fig. S26†). NMH-24 requires only 233 ± 8 and 292 ± 22 mV overpotentials to

reach 10 and 100 mA cm^{-2} (Fig. 4f and g). NMH-24 surpasses the activity of NH-24, and MH-24 which require 294, and 267 mV overpotentials at 10 mA cm^{-2}. The activity is also comparable with RuO_2 and better than that of NMH-18 and NMH-30 (Fig. S25c†). Free energy calculations corroborate the experimental results and demonstrate the best OER activity for NMH-24 (Fig. S24c and d†). Since the LSV polarization plots were recorded in a backward scan to avoid the Ni^{2+}/Ni^{3+} oxidation peak near 10 mA cm^{-2}, a negative OER current appears due to Ni^{3+} reduction to Ni^{2+}. The chronopotentiometry of NMH-24 at 10 mA cm^{-2} shows the OER overpotential to be very similar, with only a 2.4% increase than the LSV overpotential (Fig. S17f†). The Tafel slope was 42 ± 12 mV dec^{-1} with charge transfer resistance of only 6.9 Ω (Fig. S25d and e†). This activity is comparable with some of the best literature reports (Fig. S21e†).[26,27,34–37,79–84] The characterization data of NMH-24 were reproduced with the samples synthesized in multiple batches, and the catalyst durability was verified with each batch, separately with Pt wire and graphite rod counter electrodes (Fig. S23†). Since NMH-24 is directly grown on conducting Ni foam, the interfacial resistance between the electrode and lamellar structure of the catalyst is significantly lowered.[85] In

fact, blessed with easy processability and favorable water adsorption kinetics, LDH analogues are already celebrated as OER electrocatalysts.[9,15,21,86–89] The obstacle with LDH catalysts is their low operational stability, but here NMH-24 shows excellent durability for a minimum of 100 h at 20 mA cm^{-2} albeit a slight change in overpotential occurs at high current density (Fig. 4h). After 100 h, ICP-MS analysis shows the Ni : Mo atomic ratio as 20 : 1.

Water electrolysis using the Ni foam/NMH-24 ∥ Cu mesh/Cu-NW/Ni$_{73}$Mo electrode couple

When the Ni foam/NMH-24 and Cu mesh/Cu-NW/Ni$_{73}$Mo electrodes are coupled in a two-electrode alkaline electrolyzer, the cell voltage required at 10 mA cm^{-2} is 1.5 V (Fig. 6a). Here, the net experimental overpotential of 270 mV (1.5 V–1.23 V) matches well with the sum of the overpotentials from the OER (233 mV) and HER (33 mV) half-reactions, within an error limit of 4 mV. To avoid the pre-oxidation current of the metals, the LSV polarization of the electrolyzer was also conducted in backward scan mode which results in a cell voltage of 1.48 V at 10 mA cm^{-2}. From a thermodynamic perspective, the energy conversion efficiency of this electrolyzer is 100%, since a cell voltage of 1.48 V is the "thermoneutral potential" where the heat generated from the overpotential is taken up in the reaction itself and the entropy becomes zero.[21] The electrolyzer is stable for more than 200 h at a constant current density of 250 mA cm^{-2} (Fig. 6b), without interrupting the structural and morphological characteristics of the catalysts (Fig. S27 and S28†). The durability of the electrolyzer was also validated at 100 mA cm^{-2} for 100 h (Fig. S23l†). After the stability test, the electronic structure of Ni$_{73}$Mo remains almost unchanged, while the metal oxidation states are altered in the anode catalyst, NMH-24. The Ni^{2+}/Ni^{3+} ratio in NMH-24 decreases from 1.8 to 0.41 after the stability test, manifesting Ni^{3+}-based NiOOH to be the active site. In addition, Mo^{5+} partly converts to Mo^{6+} after the stability test, with Mo^{6+}/Mo^{5+} ratio of 1.21, suggesting the mixed metal oxyhydroxides with higher oxidation states as the active sites for the OER (Fig. S29†). The cell voltage of the Ni foam/NMH-24 (+) ∥ Cu mesh/Cu-NW/Ni$_{73}$Mo (−) electrode couple is found to be better or comparable with the best-reported systems (Fig. 6c).[27–30,36,38,39,71,84,86,90,91] When the electrode area is increased from 0.25 to 5 cm^2, the corresponding cell voltage expectedly increases to 1.58 V under the conditions of an industrial electrolyzer, i.e. 6 M NaOH and 80 °C, with sustained
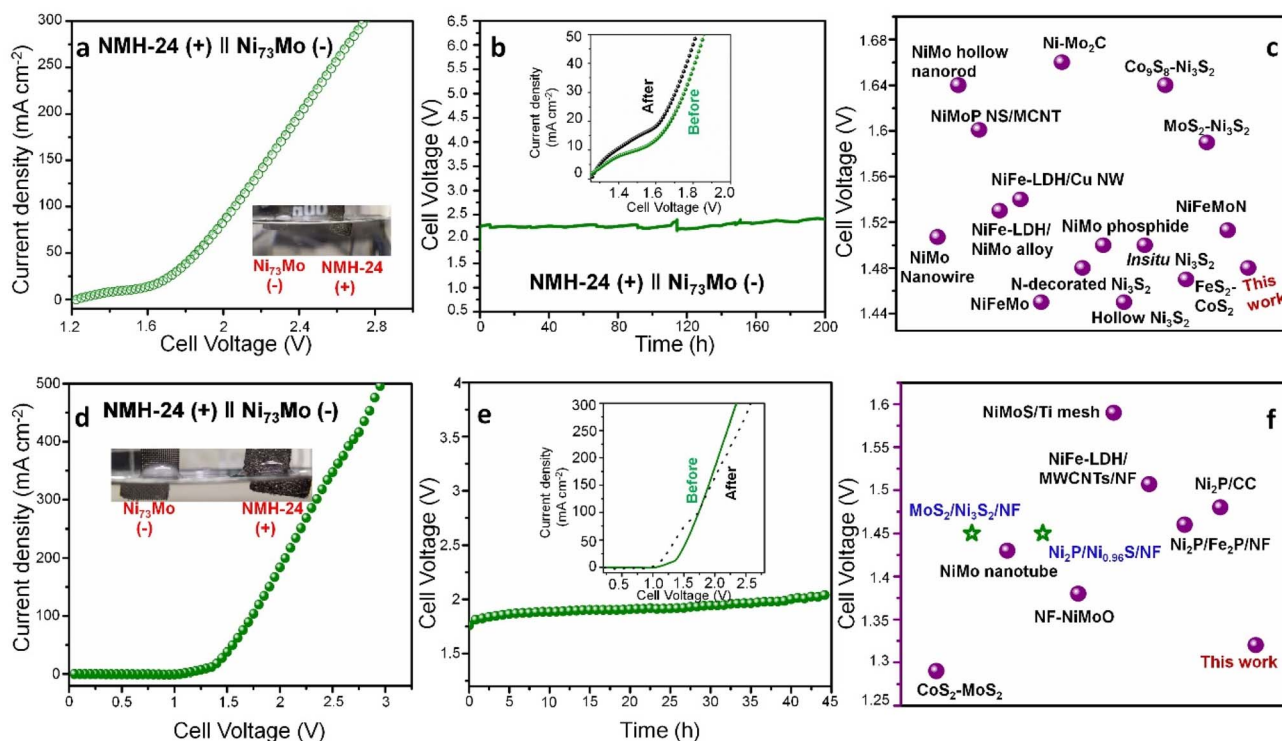
Fig. 6 Ni$_{73}$Mo and NMH-24 catalyzed water and urea electrolysis. (a) LSV polarization curves showing the overall water splitting by Ni foam/NMH-24 (+) ∥ Cu mesh/Cu-NW/Ni$_{73}$Mo (−) couple in 1 M KOH. Inset shows the digital image of the two-electrode setup. (b) Chronopotentiometry test of the Ni foam/NMH-24 (+) ∥ Cu mesh/Cu-NW/Ni$_{73}$Mo (−) electrolyzer at 250 mA cm^{-2} for 200 h. The inset shows the steady-state LSV curves before and after the stability tests. (c) Scatter plot for literature reported water-splitting cell voltages at 10 mA cm^{-2}: ref. [27] NiFeMo,[28] NiMo nanowire,[29] NiMo phosphide,[30] Ni–Mo$_2$C,[36] Co$_9$S$_8$–Ni$_3$S$_2$,[39] hollow Ni$_3$S$_2$,[40] N-doped Ni$_3$S$_2$,[41] FeS$_2$/CoS$_2$,[71] NiMo hollow nanorods,[86] NiFe-LDH/Cu-NW,[84] MoS$_2$–NiS$_2$,[90] Ni$_3$S$_2$,[91] and NiFe-LDH (+) ∥ NiMo alloy (−). (d) LSV polarization curves (iR-corrected) showing the overall urea splitting using the Ni foam/NMH-24 (+) ∥ Cu mesh/Cu-NW/Ni$_{73}$Mo (−) couple in 1 M KOH + 0.33 M urea. (e) Chronopotentiometry test of the Ni foam/NMH-24 (+) ∥ Cu mesh/Cu-NW/Ni$_{73}$Mo (−) electrolyzer for urea splitting at 100 mA cm^{-2}. The insets show steady-state LSV plots before and after the stability tests. (f) Scatter plot for literature reported urea splitting cell voltages at 10 mA cm^{-2}:[42] NF–NiMoO,[43] NiMo nanotube,[44] CoS$_2$–MoS$_2$,[45] Ni$_2$P–Fe$_2$P,[46] MoS$_2$–Ni$_3$S$_2$,[47] Ni$_2$P–Ni$_{0.96}$S,[48] NiFe-LDH/MWCNT/NF,[49] NiMo microrod,[50] NiMoS/Ti mesh,[51] and Ni$_2$P.

release of gas bubbles (ESI Movie S1†). Even with a larger electrode, a lower cell voltage could be achieved than the typical operating voltage of 1.8–2 V for commercial electrolyzers.

Urea electrolysis using the Ni foam/NMH-24 ‖ Cu mesh/Cu-NW/Ni$_{73}$Mo electrode couple

While water oxidation has a thermodynamic potential of 1.23 V, for the UOR, it is 0.37 V making H$_2$ generation at the cathode, a more feasible and pragmatic process. In a similar three-electrode configuration with an electrolyte containing 0.33 M urea and 1 M KOH, NMH-24 performs the UOR with a potential of only 1.34 ± 0.02 V *versus* RHE at 10 mA cm^{-2} (Fig. S30a†), which is 123 mV lower than the OER potential. Moreover, 0.5 A cm^{-2} current density is reached at only 1.51 V *versus* RHE. Accompanied by a low Tafel slope of 48 ± 10 mV dec^{-1}, NMH-24 shows a TOF of 2.87 s^{-1} at 1.48 V for the UOR, which is a significant improvement over the TOF for the OER (Fig. S30b and c†). The UOR mass activity is 100.8 ± 15 A g^{-1} at 1.5 V (Fig. S22c†). However, the ECSA is lower than that of the OER, and therefore the ability to lower the UOR activation energy is an intrinsic characteristic of NMH-24 (Fig. S30d and e†). In fact, the accomplishment of such a high UOR current density with low energy consumption is an uncommon feat (Fig. S30f†).[42–50] The Ni foam/NMH-24 (+) ‖ Cu mesh/Cu-NW/Ni$_{73}$Mo (−) couple performs overall urea splitting from 0.33 M urea + 1 M KOH electrolyte, at a cell voltage of 1.32 V (Fig. 6d), which is 180 mV lower than that of water electrolysis. The electrolyzer shows excellent durability (Fig. 6e) and its activity is better than most of the literature reports to date (Fig. 6f).[42–51] Although the crystal phase of both Ni$_{73}$Mo and NMH-24 remains intact after the stability test, the morphology of Ni$_{73}$Mo is affected due to the formation of CuO under harsh alkaline conditions (1 M KOH + 0.33 M urea) for almost 50 h. However, the morphology of NMH-24 remains intact under this harsh condition (Fig. S31a–d†). XPS data show that the Ni^{2+}/Ni^{3+} ratio in NMH-24 changes from 1.8 to 1.2, indicating the conversion of Ni^{2+} to Ni^{3+} due to the formation of NiOOH active site during the UOR. The Mo 3d spectra also show the incorporation of the Mo^{6+} state. In the case of Ni$_{73}$Mo, the binding energies of Ni^0 (852.4 eV) and Mo^0 (228.2 eV) remain almost unchanged along with the surface coverage of higher oxidation states (Fig. S31e–h†).

For theoretical calculation, following the experimental evidence, we have considered a Mo-doped Ni(OH)$_2$ system with a Ni : Mo ratio of 5 : 1. This system has four layers, where from the top to bottom layers, there are 2, 1, 1 and 1 Mo atoms, respectively. The last two layers with 1 Mo atom are frozen in order to resemble the bulk-like structure. We have considered the electronic adsorption energy of the reactant (CoN$_2$H$_4$) and the key intermediates (CO* and NH*) on the catalyst surface. Our calculations suggest that the reactant and CO* intermediate are adsorbed on the catalyst surface through the O-center. The NH* intermediate, however, gets absorbed at the Mo-center. The changes in electronic adsorption energy of Co(NH$_2$)$_2$*, CO* and NH* on the Mo-doped Ni(OH)$_2$ system are −0.59, 0.64 and 0.89 eV, respectively (Fig. S32 and Table S8†).

Conclusions

In summary, we have demonstrated an unusual inverse charge transfer from Mo to Ni both in the Ni$_{73}$Mo alloy electrodeposited on Cu nanowires as well as NiMo-hydroxide (Ni : Mo = 5 : 1) on Ni foam by XAFS and XPS analysis. This out-of-the-common intermetallic charge transfer has a prominent effect on the electrochemical redox reactions for generating H$_2$ fuel by water and urea splitting. The minimal Mo addition induces an expansive lattice strain of the metallic FCC Ni$_{73}$Mo alloy whereas NiMo-hydroxide with higher valence states crystallizes in the hexagonal hydrocalcite type LDH structure. Computational studies show that in the absence of an effective icosahedron geometry, the Mo-center is 9 coordinated and the Mo 4d-orbitals lie in the valence band region close to the Fermi energy. In contrast, the Ni 3d-orbitals remain in the conduction band near the Fermi energy. Since the undercoordinated electron-rich Mo-center donates the electron to the electron-poor Ni-center, the Mo-center accumulates a positive charge surrounded by the neighboring negatively charged Ni-centers, providing strong evidence of the inverse charge transfer. Ni$_{73}$Mo accelerates the electrochemical HER with nominal overpotentials of 33 ± 10 and 54 ± 8 mV in alkaline and acidic media at −10 mA cm^{-2}. The TOF of Ni$_{73}$Mo is 0.35 and 0.07 H$_2$ s^{-1} at 33 and 54 mV, in alkaline and acidic media, respectively, with a mass activity of 10.5 ± 2 and 2.9 ± 0.3 A g^{-1} at 100, and 54 mV overpotential, respectively. Free energy calculations show that during alkaline HER, the Mo-center acts as the active site for H$_2$O adsorption, followed by the dissociation of water on Mo- and neighboring two Ni-centers. The anodic potential overwhelms the intrinsic charge transfer direction and increases the abundance of the Ni^{3+} state in NiMo-hydroxide (NMH-24), which catalyzes the OER half-reaction with overpotentials of 233 ± 8 and 292 ± 22 mV at 10 and 100 mA cm^{-2}, TOF of 2.32 O$_2$ s^{-1} at 370 mV and mass activity of 19 ± 8 A g^{-1} at 300 mV overpotential, in alkaline medium. The remarkable water-splitting activity of this homologous couple is evident from its cell voltage of 1.48 ± 0.02 V at 10 mA cm^{-2} (backward scan) and its pristine durability at high current densities. While NMH-24 can oxidize urea at a nominal potential of 1.34 ± 0.02 V and mass activity of 100.8 ± 15 A g^{-1} at 1.5 V *versus* RHE, the homologous couple performs urea splitting at only 1.32 ± 0.02 V at 10 mA cm^{-2}.

Experimental section

Materials

Cu mesh, Ni foam (Alfa Aesar, 0.11 mm), nickel(II) sulphate heptahydrate (Ni(SO$_4$)$_2$·7H$_2$O; Merck, ≥98%), potassium hydrogen carbonate (KHCO$_3$; Merck, ≥99.5%), ammonium persulphate (Lobachemie, ≥98%), ammonia solution (Merck, ≥25%), nickel(II) chloride hexahydrate (NiCl$_2$·6H$_2$O; Merck, ≥99%), sodium hydroxide (NaOH; Merck, ≥97%), potassium hydroxide pellets (KOH; Merck, ≥85%), ethanol (C$_2$H$_5$OH; Merck ≥99.9%), Toray carbon fiber paper (CFP; Alfa Aesar), carbon cloth (Alfa Aesar), commercial Pt/C (20 wt%, Merck), ruthenium oxide (RuO$_2$; Merck), ammonium heptamolybdate

tetrahydrate ($(NH_4)_6Mo_7O_{24} \cdot 4H_2O$; 97%, Merck), sodium chloride (NaCl; 99%, Merck), sodium hydrogen citrate ($Na_2C_6H_6O_7$; 98%, Merck), nickel nitrate hexahydrate ($Ni(NO_3)_2 \cdot 6H_2O$; 98%, Merck), iron nitrate nonahydrate ($Fe(NO_3)_3 \cdot 9H_2O$; 98%, Merck), were used without further purification, except for Ni foam and Cu mesh.

Preparation of the self-supported Cu-m/Cu-NW electrode

Following our previous protocol,[15] $Cu(OH)_2$ nanowires were first grown on Cu mesh followed by its conversion to Cu-NW. The cleaned Cu mesh electrodes of 3×0.5 cm^2 area were dipped in a 14 mL aqueous solution of 0.84 g NaOH and 0.24 g $(NH_4)_2S_2O_8$ to form the $Cu(OH)_2$ nanowires supported on Cu mesh. $Cu(OH)_2$ was subjected to air oxidation at 180 °C to form CuO nanowires. Self-supported Cu-NW were prepared by electrochemical reduction of the CuO nanowires at -1.08 V versus Ag/AgCl in 1 M KHCO$_3$ with Pt as the counter electrode and Ag/AgCl (3 M KCl) as the reference electrode.

Synthesis of Ni$_{73}$Mo and analogues on the Cu-m/Cu-NW electrode

The Ni$_{73}$Mo alloy was electrodeposited onto Cu-m/Cu-NW substrates in a galvanostatic mode in an electrolyte consisting of 0.017 M $Ni(SO_4)_2 \cdot 7H_2O$, 0.016 M $Na_3C_6H_5O_7$, 0.36 mM $(NH_4)_6Mo_7O_{24} \cdot 4H_2O$, and 0.28 M NaCl in 40 mL DI water. 27 wt% aqueous NH$_3$ solution was added to maintain the pH ~9.5. Cu-m/Cu-NW was the working electrode in a three-electrode set-up, alongside a Pt wire and Ag/AgCl (3 M KCl) as counter and reference electrodes, respectively. The electrodeposition was carried out at -100 mA cm^{-2} for 1 h to make Ni$_{73}$Mo. The alloy analogues were prepared by varying the electrodeposition time to 30- and 90 min and current densities to -50 and -200 mA cm^{-2}. The electrodes were dried overnight under vacuum followed by washing multiple times with DI water. Different catalyst loadings were obtained by changing the deposition time and current density. Ni-100-60m and Mo-100-60m were synthesized keeping similar conditions to that of Ni$_{73}$Mo, except with only Mo- and Ni-salt, respectively.

Synthesis of NMH-t on Ni foam

At first, the Ni foam electrodes were washed with concentrated HCl and water. The Ni foam electrodes of 0.5×1 cm^2 area were dipped in a 50 mL aqueous electrolyte containing 0.48 g $NiCl_2 \cdot 6H_2O$, 0.05 g $(NH_4)_6Mo_7O_{24}$ and 0.11 g NH$_4$Cl followed by potentiostatic deposition under -1.7 V versus Ag/AgCl for different time periods of 6, 12, 18, 24, 30 min.[9,21] Ni- and Mo-only hydroxides (NH-24 and MH-24) were electrodeposited for 24 min under the same potential taking only Ni- and Mo-salt, respectively.

Physical characterization

XRD measurements were conducted on a Rigaku (mini flex II, Japan) powder X-ray diffractometer with Cu Kα radiation with 1° min^{-1} scan rate. FESEM images and EDX spectra were obtained using a Carl Zeiss SUPRA 55VP and an Oxford

Instruments X-Max system with INCA software, respectively. Rietveld analysis of the XRD patterns was conducted with General Structure Analysis System (GSAS) software (Los Angeles National Laboratory Report, 2004). The structures of the alloy and hydroxides were drawn in Vesta software. Strain calculations were performed using strain++ software. TEM images of Ni$_{73}$Mo on Cu-NW were taken directly on the substrate using a JEOL, JEM-2100F microscope with a 200 kV electron source at the DST-FIST facility, IISER Kolkata. For the NMH-24 catalyst, the TEM images were taken on Cu grids after scratching it from the Ni foam followed by dispersing the powder in isopropanol. Ni and Mo K-edge XAFS spectra were recorded at BL-9, Scanning XAFS Beamline of Indus-2, RRCAT, Indore. XAFS measurements were done in fluorescence mode for Ni and Mo K-edges using a Vortex energy dispersive detector. The beamline mainly consists of a Rh/Pt coated meridional cylindrical mirror for collimation and a Si (111) based double crystal monochromator to select the excitation energy. The energy range of XAFS was calibrated using Ni and Mo metal foil pieces. The normalized XANES data and R spectra were collected from the absorption spectra using ATHENA software. On a commercial photoelectron spectrometer PHI 5000 Versa ProbeII, FEI Inc, the XPS studies were carried out by mounting the samples on copper stubs with silver paste using an Al Kα (1486.6 eV) excitation source. The acquired data were background-corrected by the Shirley method, followed by fitting with Fityk software, with Voigt peaks having 80% Gaussian and 20% Lorentzian components. C correction was done for all the data with the reference peak of 284.8 eV of the C–C bond. The stoichiometry determination by inductively coupled plasma optical emission spectroscopy was performed with a Thermo Fisher Scientific IC74DC 193405. ICP-MS analyses were performed with a Thermo Scientific XSeries 2 ICPMS instrument.

Calculation of lattice strain

Lattice strain was calculated from the Williamson–Hall (W–H) plot according to eqn (1):[52]

$$\beta\cos\theta = \frac{k\lambda}{D} + 4\varepsilon\sin\theta \tag{1}$$

where β is the full-width at half maximum for all the diffraction planes, k is the Scherrer constant ($= 0.9$), D is the particle size and ε is the intrinsic lattice strain.

Electrochemical measurements

In a Biologic VSP-300 electrochemical workstation, the electrochemical characterization studies were carried out with a three-electrode set-up for the half-reactions and a two-electrode set-up for overall water and urea splitting. The alkaline OER and HER performances in 1 M KOH were evaluated with the self-supported working electrode clamped to the Ni foam/Cu mesh substrates, a graphite rod as the counter electrode and Hg/HgO as the reference electrode. In an acidic electrolyte (0.5 M H$_2$SO$_4$), the HER activity was studied with a Pt wire and calomel electrode as the counter and reference electrodes, respectively. The loading of the catalysts on self-supported electrodes was

obtained from the weight difference of the electrode before and after electrodeposition. The catalyst loading of the NiMo alloy on Cu-NW was 4 mg cm^{-2} whereas the catalyst loading of NiMo hydroxides on Ni foam was 4.5 mg cm^{-2}. For effective comparison, the loading of 20% Pt/C in Cu mesh and RuO$_2$ in Ni foam was also maintained as 4 and 4.5 mg cm^{-2}, respectively. The current density for all the measurements was calculated considering the working surface area from a single side of the electrode. All the potentials in the three-electrode measurements were 85% *iR*-corrected to compensate for the effect of solution resistance unless specified and calibrated to RHE. For the OER, LSV measurements were taken at a scan rate of 1 mV s^{-1} in a backward scan to avoid the pre-redox peak of Ni^{2+} to higher oxidation states and also to minimize the capacitive current. The LSV polarization was also conducted in backward scan mode to avoid any reduction of metals, during HER measurements. For overall urea splitting, LSV measurements were taken at a scan rate of 5 mV s^{-1} in backward scan for resolving similar issues. For overall water splitting, the LSV measurements were taken at a scan rate of 5 mV s^{-1} in a forward scan as the oxidation peak is appearing before the current density of 10 mA cm^{-2}. The LSV polarization was also conducted in backward scan mode for the overall electrolyzer at the same scan rate. To increase the hydrophilicity of the electrodes and stabilize the electrocatalytic activity, all the working electrodes were saturated by 20 CV scans at a scan rate of 200 mV s^{-1}. Gas chromatographic measurement of Ni$_{73}$Mo was performed on a Thermo Fisher GC Trace 1110 instrument by chronoamperometry at 138 mV overpotential for 10 min with a discharge ionization detector (DID) using He as the carrier gas. The durability tests in 1 M KOH were separately performed using a Pt wire and graphite rod as counter electrodes.

Mott–Schottky measurements of the OER catalysts were performed in the potential range −0.93 V to 3.2 V *versus* RHE in the frequency range between 1 MHz and 100 Hz. Flat band potential (E_{fb}) and dopant density (N_d) were calculated by fitting the Mott–Schottky plot according to eqn (2):[56]

$$\frac{1}{C_s^2} = \frac{2}{\varepsilon\varepsilon_0 A^2 e N_d}\left(E - E_{fb} - \frac{k_B T}{e}\right) \quad (2)$$

where C_s is the differential capacitance $\partial Q/\partial E$, ε and ε_0 are the dielectric constants of the semiconductor and the permittivity of free space (8.85×10^{-12} F m^{-1}), respectively, A is the area, e is the elementary charge (1.6×10^{-19} C), E is the applied potential (specific to the electrode), k_B is Boltzmann constant (1.38×10^{-23} J K^{-1}) and T is the absolute temperature (298 K). The fitting of the Mott–Schottky plot was done in EC lab software. EIS studies were performed at an overpotential of 234 and 336 mV in 1 M KOH for the HER and OER, respectively, in order to compare the charge transfer resistance (R_{CT}) in the faradaic region. R_{CT} is inversely proportional to the rate of charge transfer. The value of R_{CT} was determined from Z-fit software by fitting the Nyquist plot. Faradaic efficiency was measured by using the eudiometric method in an air-tight vessel. The double layer capacitance (C_{dl}) of OER catalysts was obtained by collecting CV scans at 20, 40, 60 and 80 mV s^{-1} in the non-faradaic region (−0.02 to +0.02 V *versus* open circuit voltage). C_{dl} measurements of HER catalysts were

conducted by collecting the same CV scans in the non-faradaic region (−0.05 to +0.05 V *versus* open circuit voltage). The ECSA of these catalysts was determined by dividing the C_{dl} by specific capacitance (0.04 mF cm^{-2}). TOF was calculated at different potentials following our previous report.[71]

Computational studies

Spin-polarized DFT simulations were carried out using the Vienna *ab initio* simulation package (VASP).[58,59] The exchange-correlation functional considered here is generalized gradient approximation (GGA) based Perdew–Burke–Ernzerhof (PBE) functional.[59,60] All structural models were relaxed until the ionic Hellmann–Feynman forces were smaller than 0.02 meV Å^{-1}. The frozen-core projector-augmented wave (PAW) method was used to describe the interactions between core electrons and valence electrons. Wave functions were expanded on a plane wave basis with high energy using the plane-wave cutoff energy of 400 eV. In order to prevent interaction between slabs, a vacuum gap of 12 Å was added along the *z*-direction. An 80 atom, 6-layers of (4 × 4) Ni (111) slice was created from the bulk-relaxed structure of Ni. A surface Ni-atom was substituted with a Mo resulting in a Ni : Mo ratio of 79 : 1 which is close to the experimentally synthesized system with a 73 : 1 ratio. We considered the Volmer step for the theoretical modeling of the HER in the alkaline medium. The Volmer and Tafel steps can be written as:

$$H_2O + {}^* + e^- \rightarrow H^* + OH^- \text{ (Volmer step)} \quad (3)$$

$$2H^* + 2e^- \rightarrow H_2 \text{ (Tafel Step)} \quad (4)$$
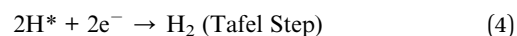
The asterisks here denote the catalyst surface and adsorbed species on the surface. Gibbs free energy (ΔG) for each adsorbate was calculated using eqn (5):

$$\Delta G = \Delta E + \Delta ZPE - T\Delta S - neU \quad (5)$$

where ΔE is the adsorption energy, T is the temperature, ΔE_{ZPE} is the difference in the zero-point energy, ΔS is the entropy change, U is the applied potential and n is the number of charges involved in a particular reaction step. As suggested from eqn (5), the electrode potential is a constant term which will make a linear shift in the overall free energy values leaving the nature of the curve unchanged. Hence, we have considered $U = 0$ V potential for all the steps. As the vibration entropy of the adsorbed H* is small, the entropy of adsorption of $\frac{1}{2}H_2$ is considered as $\Delta S_H \sim 1/2 S_{H_2}^\circ$, where $1/2 S_{H_2}^\circ$, is the entropy of H$_2$ in the gas phase under standard conditions. So, in order to calculate the free energy of each structure, we have added ΔZPE, which is calculated by taking the Hessian matrix into account. We have also considered the entropic aspect. However, we have not considered the rotational and transitional vibrations explicitly.

Data availability

The datasets supporting this study are available from the authors upon reasonable request and other relevant information is given in the provided ESI.†

Author contributions

S. P., M. Mj., and A. K. synthesized and characterized the nanostructures, and performed the electrochemical measurements. N. B., S. D., and S. K. P. performed the computational studies. M. M. helped in synthesis and characterization. D. K. C., P. R., M. K. performed the XAFS measurements. S. P. analyzed the data. S. P. and S. B. conceived the study. S. P., N. B., S. D., S. K. P. and S. B. co-wrote the paper.

Conflicts of interest

There are no conflicts of interest to declare.

Acknowledgements

References

1 J. Masa, C. Andronescu and W. Schuhmann, *Angew. Chem., Int. Ed.*, 2020, **59**, 15298.

2 X. Tao, Y. Wang, Y. Zou, N. Zhang, Y. Zhang, Y. Wu, Y. Wang, R. Chen and S. Wang, *Adv. Energy Mater.*, 2020, **10**, 1901227.

3 D. Yi, F. Lu, F. Zhang, S. Liu, B. Zhou, D. Gao, X. Wang and J. Yao, *Angew. Chem., Int. Ed.*, 2020, **132**, 15989.

4 X. Xiao, L. Tao, M. Li, X. Lv, D. Huang, X. Jiang, H. Pan, M. Wang and Y. Shen, *Chem. Sci.*, 2018, **9**, 1970–1975.

5 L. Pauling, *J. Am. Chem. Soc.*, 1932, **54**, 3570–3582.

6 J. Hinze, M. Whitehead and H. Jaffé, *J. Am. Chem. Soc.*, 1963, **85**, 148–154.

7 E. Gyftopoulos and G. Hatsopoulos, *Proc. Natl. Acad. Sci. U. S. A.*, 1968, **60**, 786–793.

8 F. Lin, Z. Dong, Y. Yao, L. Yang, F. Fang and L. Jiao, *Adv. Energy Mater.*, 2020, **10**, 2002176.

9 S. Parvin, V. Hazra, A. Francis, S. Pati and S. Bhattacharyya, *Inorg. Chem.*, 2021, **60**, 6911–6921.

10 G. Hai, J. Huang, L. Cao, K. Kajiyoshi, L. Wang and L. Feng, *Appl. Surf. Sci.*, 2021, **562**, 150145.

11 K. Liu, C. Zhang, Y. Sun, G. Zhang, X. Shen, F. Zou, H. Zhang, Z. Wu, E. Wegener and C. Taubert, *ACS Nano*, 2017, **12**, 158–167.

12 Z. Xue, S. Zhang, Y. Lin, H. Su, G. Zhai, J. Han, Q. Yu, X. Li, M. Antonietti and J. Chen, *J. Am. Chem. Soc.*, 2019, **141**, 14976–14980.

13 R. Majee, A. Kumar, T. Das, S. Chakraborty and S. Bhattacharyya, *Angew. Chem., Int. Ed.*, 2020, **59**, 2881–2889.

14 Q. Yan, D. Wu, S. Chu, Z. Chen, Y. Lin, M. Chen, J. Zhang, X. Wu and H. Liang, *Nat. Commun.*, 2019, **10**, 4977.

15 S. Parvin, A. Kumar, A. Ghosh and S. Bhattacharyya, *Chem. Sci.*, 2020, **11**, 3893–3902.

16 Y. Peng, B. Lu, N. Wang, L. Li and S. Chen, *Phys. Chem. Chem. Phys.*, 2017, **19**, 9336–9348.

17 J. Tian, Q. Liu, A. Asiri and X. Sun, *J. Am. Chem. Soc.*, 2014, **136**, 7587–7590.

18 M. Ming, Y. Ma, Y. Zhang, L. Huang, L. Zhao, Y. Chen, X. Zhang, G. Fan and J. Hu, *J. Mat. Chem. A*, 2018, **6**, 21452–21457.

19 Z.-W. Wei, H.-J. Wang, C. Zhang, K. Xu, X.-L. Lu and T.-B. Lu, *Angew. Chem., Int. Ed.*, 2021, **60**, 16622–16627.

20 N. Padma, S. Thomas, C. A. Betty, R. Rao, N. Gupta, K. G. Girija and J. Jagannath, *Appl. Surf. Sci.*, 2021, **542**, 148743.

21 A. Sahasrabudhe, H. Dixit, R. Majee and S. Bhattacharyya, *Nat. Commun.*, 2018, **9**, 2014.

22 J. Zhang, T. Wang, P. Liu, Z. Liao, S. Liu, X. Zhuang, M. Chen, E. Zschech and X. Feng, *Nat. Commun.*, 2017, **8**, 15347.

23 Y. Chen, Y. Zhang, X. Zhang, T. Tang, H. Luo, S. Niu, Z. Dai, L. Wan and J. Hu, *Adv. Mater.*, 2017, **29**, 1703311.

24 S. Zhao, J. Huang, Y. Liu, J. Shen, H. Wang, X. Yang, Y. Zhu and C. Li, *J. Mater. Chem. A*, 2017, **5**, 4207–4214.

25 M. Gao, C. Yang, Q. Zhang, J. Zeng, X. Li, Y. Hua, C. Xu and P. Dong, *J. Mater. Chem. A*, 2017, **5**, 5797–5805.

26 C. Zhu, Z. Yin, W. Lai, Y. Sun, L. Liu, X. Zhang, Y. Chen and S. L. Chou, *Adv. Energy Mater.*, 2018, **8**, 1802327.

27 F. Qin, Z. Zhao, M. K. Alam, Y. Ni, F. Robles-Hernandez, L. Yu, S. Chen, Z. Ren, Z. Wang and J. Bao, *ACS Energy Lett.*, 2018, **3**, 546–554.

28 Y. Wang, Y. Sun, F. Yan, C. Zhu, P. Gao, X. Zhang and Y. J. Chen, *Mater. Chem. A*, 2018, **6**, 8479–8487.

29 H. Xu, J. Wei, K. Zhang, Y. Shiraishi and Y. K. Du, *ACS Appl. Mater. Interfaces*, 2018, **10**, 29647–29655.

30 Z. Y. Yu, Y. Duan, M. R. Gao, C. C. Lang, Y. R. Zheng and S. H. Yu, *Chem. Sci.*, 2017, **8**, 968–973.

31 L. Li, Y. Li and Z. Liu, *ACS Catal.*, 2020, **10**, 2581–2590.

32 J. Lai, B. Huang, Y. Chao, X. Chen and S. Guo, *Adv. Mater.*, 2018, **31**, 1805541.

33 A. Kumar, X. Liu, J. Lee, B. Debnath, A. Jadhav, X. Shao, V. Bui, Y. Hwang, Y. Liu, M. Kim and H. Lee, *Energy Environ. Sci.*, 2021, **14**, 6494–6505.

34 Y. Jia, L. Z. Zhang, G. P. Gao, H. Chen, B. Wang, J. Z. Zhou, M. T. Soo, M. Hong, X. C. Yan, G. R. Qian, J. Zou, A. J. Du and X. D. Yao, *Adv. Mater.*, 2017, **29**, 1700017.

35 B. You, N. Jiang, M. Sheng, M. W. Bhushan and Y. Sun, *ACS Catal.*, 2016, **6**, 714–721.

36 F. Du, L. Shi, Y. Zhang, T. Li, J. Wang, G. Wen, A. Alsaedi, T. Hayat, Y. Zhou and Z. Zou, *Appl. Catal., B*, 2019, **253**, 246–252.

37 Y. Jin, X. Yue, C. Shu, S. Huang and P. Shen, *J Mater. Chem. A*, 2017, **5**, 2508–2513.

38 Y. Wang, L. Pan, Y. Chen, G. Shen, L. Wang, X. Zhang and J. Zou, *Int. J. Hydrogen Energy*, 2020, **45**, 15560–15570.

39 Y. Wu, G. D. Li, Y. Liu, L. Yang, X. Lian, T. Asefa and X. Zou, *Adv. Funct. Mater.*, 2016, **26**, 4839–4847.

40 P. Chen, T. Zhou, M. Zhang, Y. Tong, C. Zhong, N. Zhang, L. Zhang, C. Wu and Y. Xie, *Adv. Mater.*, 2017, **29**, 1701584.

41 Y. Li, J. Yin, L. An, M. Lu, K. Sun, Y. Zhao, D. Gao, F. Cheng and P. Xi, *Small*, 2018, **14**, 1801070.

42 Z. Yu, C. Lang, M. Gao, Y. Chen, Q. Fu, Y. Duan and S. Yu, *Energy Environ. Sci.*, 2018, **11**, 1890–1897.

43 J. Zhang, T. He, M. Wang, R. Qi, Y. Yan, Z. Dong, H. Liu, H. Wang and B. Xia, *Nano Energy*, 2019, **60**, 894–902.

44 C. Li, Y. Liu, Z. Zhuo, H. Ju, D. Li, Y. Guo, X. Wu, H. Li and T. Zhai, *Adv. Energy Mater.*, 2018, **8**, 1801775.

45 L. Yan, Y. L. Sun, E. L. Hu, J. Q. Ning, Y. J. Zhong, Z. Y. Zhang and Y. J. Hu, *Colloids Interface Sci.*, 2019, **541**, 279–286.

46 F. Li, J. Chen, D. Zhang, W.-F. Fu, Y. Chen, Z. Wen and X. J. Lv, *Chem. Commun.*, 2018, **54**, 5181–5184.

47 M. He, C. Feng, T. Liao, S. Hu, H. Wu and Z. Sun, *ACS Appl. Mater. Interfaces*, 2020, **12**, 2225–2233.

48 X. Wen, *Int. J. Hydrogen Energy*, 2020, **45**, 14660–14668.

49 J. Cao, H. Li, R. Zhu, L. Ma, K. Zhou, Q. Wei and F. Luo, *J. Alloys Compd.*, 2020, **844**, 338–347.

50 X. Wang, J. Wang, X. Sun, S. Wei, L. Cui, W. Yang and J. Liu, *Nano Res.*, 2018, **11**, 988–996.

51 X. Zhang, Y. Liu, Q. Xiong, G. Liu, C. Zhao, G. Wang, Y. Zhang, H. Zhang and H. Zhao, *Electrochim. Acta*, 2017, **254**, 44–49.

52 A. Mandal, A. Ghosh, S. P. Senanayak, R. H. Friend and S. Bhattacharyya, *J. Phys. Chem. Lett.*, 2021, **12**, 1560–1566.

53 S. Bhattar, M. Abedin, D. Shekhawat, D. Haynes and J. Spivey, *Appl. Catal., A*, 2020, **602**, 117721.

54 D. Cao, K. Ye, O. Moses, W. Xu, D. Liu, P. Song, C. Wu, C. Wang, S. Ding, S. Chen, B. Ge, J. Jiang and Li. Song, *ACS Nano*, 2019, **13**, 11733–11740.

55 K. Gelderman, L. Lee and S. W. Donne, *J. Chem. Educ.*, 2007, **84**, 685–688.

56 R. Majee, S. Mondal and S. Bhattacharyya, *Chem. Commun.*, 2020, **56**, 8277–8280.

57 X. Cheng, E. Fabbri, Y. Yamashita, I. Castelli, B. Kim, M. Uchida, R. Haumont, I. Puente-Orench and T. Schmidt, *ACS Catal.*, 2018, **8**, 9567–9578.

58 G. Kresse and J. Furthmüller, *Phys. Rev. B: Condens. Matter Mater. Phys.*, 1996, **54**, 11169–11186.

59 G. Kresse and D. Joubert, *Phys. Rev. B: Condens. Matter Mater. Phys.*, 1999, **59**, 1758–1775.

60 J. P. Perdew, K. Burke and M. Ernzerhof, Generalized Gradient Approximation Made Simple, *Phys. Rev. Lett.*, 1996, **77**, 3865–3868.

61 L. Rößner, H. Schwarz, I. Veremchuk, R. Zerdoumi, T. Seyller and M. Armbrüster, *ACS Appl. Mater. Interfaces*, 2021, **13**, 23616–23626.

62 P. E. Blöchl, *Phys. Rev. B: Condens. Matter Mater. Phys.*, 1994, **50**, 17953–17979.

63 W. Tang, E. Sanville and G. A. Henkelman, *J. Phys.: Condens. Matter*, 2009, **21**, 084204.

64 T. Cadenbach, T. Bollermann, C. Gemel, I. Fernandez, M. von Hopffgarten, G. Frenking and R. A. Fischer, *Angew. Chem., Int. Ed.*, 2008, **47**, 9150–9154.

65 A. Kumar and S. Bhattacharyya, *ACS Appl. Mater. Interfaces*, 2017, **9**, 4190641915.

66 W. Sun, Z. Q. Wang, W. Q. Zaman, Z. H. Zhou, L. M. Cao, X. Q. Gong and J. Yang, *Chem. Commun.*, 2018, **54**, 996–999.

67 Y. Wang, G. Zhang, W. Xu, P. Wan, Z. Lu, Y. Li and X. Sun, *ChemElectroChem*, 2014, **1**, 1089.

68 D. Rodene, E. Eladgham, R. Gupta, I. Arachchige and V. Tallapally, *ACS Appl. Energy Mater.*, 2019, **2**, 7112–7120.

69 Y. Zhou, M. Luo, W. Zhang, Z. Zhang, X. Meng, X. Shen, H. Liu, M. Zhou and X. Zeng, *ACS Appl. Mater. Interfaces*, 2019, **11**, 21998–22004.

70 Q. Zhang, P. Li, D. Zhou, Z. Chang, Y. Kuang and X. Sun, *Small*, 2017, **13**, 1701648.

71 J. Tian, N. Cheng, Q. Liu, X. Sun, Y. He and A. Asiri, *J. Mater. Chem. A*, 2015, **3**, 20056–20059.

72 J. McKone, B. Sadtler, C. Werlang, N. Lewis and H. Gray, *ACS Catal.*, 2013, **3**, 166–169.

73 Y. Chen, C. Dong, J. Zhang, C. Zhang and Z. Zhang, *J. Mater. Chem. A*, 2018, **6**, 8430–8440.

74 Y. Ito, T. Ohto, D. Hojo, M. Wakisaka, Y. Nagata, L. Chen, K. Hu, M. Izumi, J. Fujita and T. Adschiri, *ACS Catal.*, 2018, **8**, 3579–3586.

75 J. Park, J. Kim, G. Han, J. Kim, S. Yoo, H. Kim and S. Ahn, *J. Mat. Chem. A*, 2021, **9**, 3677–3684.

76 Z. Chang, L. Zhu, J. Zhao, P. Chen, D. Chen and H. Gao, *Int. J. Hydrogen Energy*, 2021, **46**, 3493–3503.

77 T. Wang, X. Wang, Y. Liu, J. Zheng and X. Li, *Nano Energy*, 2016, **22**, 111–119.

78 F. Bao, E. Kemppainen, I. Dorbandt, R. Bors, F. Xi, R. Schlatmann, R. Krol and S. Calnan, *ChemElectroChem*, 2021, **8**, 195–208.

79 A. Sivanantham, P. Ganesan and S. Shanmugam, *Adv. Funct. Mater.*, 2016, **26**, 4661–4672.

80 C. Du, L. Yang, F. L. Yang, G. Z. Cheng and W. Luo, *ACS Catal.*, 2017, **7**, 4131.

81 G. B. Darband, M. Aliofkhazraei, S. Hyun, A. S. Rouhaghdam and S. Shanmugam, *Nanoscale*, 2019, **11**, 16621–16634.

82 H. Huang, C. Yu, C. Zhao, X. Han, J. Yang, Z. Liu, S. Li, M. Zhang and J. Qiu, *Nano Energy*, 2017, **34**, 472–480.

83 Z. Yan, E. Wang, J. Gao, J. Yang, C. Wu, L. Jiang, M. Zhu and G. Sun, *ChemElectroChem*, 2017, **4**, 2190–2195.

84 J. Lin, P. Wang, H. Wang, C. Li, X. Si, J. Qi, J. Cao, Z. Zhong, W. Fei and J. Feng, *Adv. Sci.*, 2019, **6**, 1900246.

85 L. B. Wu, L. Yu, X. Xiao, F. H. Zhang, S. W. Song, S. Chen and Z. F. Ren, *Research*, 2020, **2020**, 3976278.

86 L. Yu, H. Zhou, J. Sun, F. Qin, F. Yu, J. Bao, Y. Yu, S. Chen and Z. Ren, *Energy Environ. Sci.*, 2017, **10**, 1820–1827.

87 S. Parvin, D. Chaudhary, A. Ghosh and S. Bhattacharyya, *ACS Appl. Mater. Interfaces*, 2019, **11**, 30682–30693.

88 R. Majee, Q. Islam and S. Bhattacharyya, *ACS Appl. Mater. Interfaces*, 2019, **11**, 35853–35862.

89 S. Mondal, R. Majee, Q. Arif Islam and S. Bhattacharyya, *ChemElectroChem*, 2020, **7**, 5005–5012.

90 M. Guo, A. Qayum, S. Dong, X. Jiao, D. Chen and T. J. Wang, *J. Mater. Chem. A*, 2020, **8**, 9239–9247.

91 M. Fang, W. Gao, G. Dong, Z. Xia, S. Yip, Y. Qin, J. C. Ho and Y. Qu, *Nano Energy*, 2016, **27**, 247–254.